Soft Matter

PAPER

View Article Online
View Journal

Cite this: DOI: 10.1039/c7sm00131b

Buckling of elastomer sheets under non-uniform electro-actuation

Hadrien Bense, * Miguel Trejo, Etienne Reyssat, José Bico and Benoît Roman

Received 19th January 2017,
Accepted 23rd March 2017

DOI: 10.1039/c7sm00131b

rsc.li/soft-matter-journal

Dielectric elastomer sheets undergo in-plane expansion when stimulated by a transverse electric field. We study experimentally how dielectric plates subjected to a non-uniform voltage distribution undergo buckling instabilities. Two different configurations involving circular plates are investigated: plates freely floating on a bath of water, and plates clamped on a frame. We describe theoretically the out-of-plane deformation of the plates within the framework of weakly non-linear plate equations. This study constitutes a first step of a route to control the 3D activation of dielectric elastomers.

1 Introduction

Dielectric actuation was discovered in the 1880s by W. Röntgen,[1] but practical studies have started flourishing only recently after the seminal work from Pelrine *et al.*[2] In dielectric actuation, the opposing sides of a sheet of elastomer are coated with compliant electrodes. Applying a high voltage V to this soft capacitor tends both to compress the membrane across its thickness and to stretch its surface (Fig. 1). In contrast with piezoelectric ceramics, dielectric elastomers can undergo very high strains of up to 500%,[3] which have inspired numerous potential applications ranging from bioinspired actuators[4,5] to soft grippers,[6,7] bearing-free motors[8] or energy harvesting systems.[9,10] However, dielectric elastomers are prone to electromechanical instabilities when high electric fields are applied. Thinning down the membrane indeed results in higher electric fields (for a fixed applied voltage) which amplifies the actuation and eventually leads to a "pull-in" instability and electrical breakdown.[11,12] A common solution to avoid this destructive instability consists in strongly prestretching the membrane (up to 300%, depending on the elastomer used). Due to the non-linear elastic properties, the polymer stiffens when prestretched, which prevents the pull-in instability. Other types of instabilities are nevertheless common. Impressive shape bifurcations can for instance be observed in pressurised membranes.[13–16] Harnessing buckling instabilities is moreover a key for many potential applications such as dynamic surface patterning,[17,18] flow regulation in micro-fluidic devices,[19] tuning of variable focal lenses[20] or haptic displays (*e.g.* Braille screens).[21,22]

Laboratoire de Physique et Mécanique des Milieux Hétérogènes (PMMH), CNRS, ESPCI Paris, PSL Research University, Sorbonne Université, Univ. Paris Diderot. Paris, France. E-mail: hadrien.bense@espci.fr

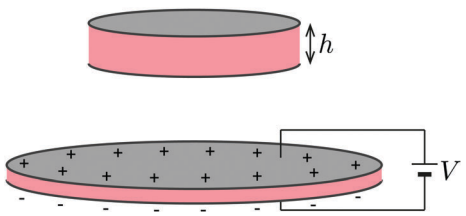

Fig. 1 Principle of dielectric actuation. A membrane of the dielectric elastomer (polyvinylsiloxane) is coated with conductive powder (carbon black) on both sides. As an electric field is applied to the membrane, the attraction between opposite charges on both sides and the repulsion of charges of the same sign on each side both tend to squeeze and stretch the membrane.

In the present study, we propose to investigate how a non-uniform spatial distribution of the applied voltage induces different out-of-plane buckling patterns. In contrast to most studies, buckling is here not due to the clamped edges of the polymer, but only to the inhomogeneous actuation of the membrane. Our experiments are inspired by recent works on the non-uniform growth of plant leaves or material swelling that leads to complex 3D shapes.[23–25] The present study thus constitutes a first step towards 3D electrical morphing. Spectacular strains are generally obtained by applying strong mechanical tension prior to actuation. However, since such prestrains would hinder the formation of 3D shapes we do not apply any significant pre-stretch to the membrane.

We focus on model axisymmetric configurations where active circular domains are surrounded by passive materials with well-defined boundary conditions. Actuation is therefore non-homogeneous as one region is subjected to voltage while the rest of the membrane is not. In the first configuration, the membrane floats freely at the surface of a bath of water that plays the role of the counter-electrode (Fig. 2a).

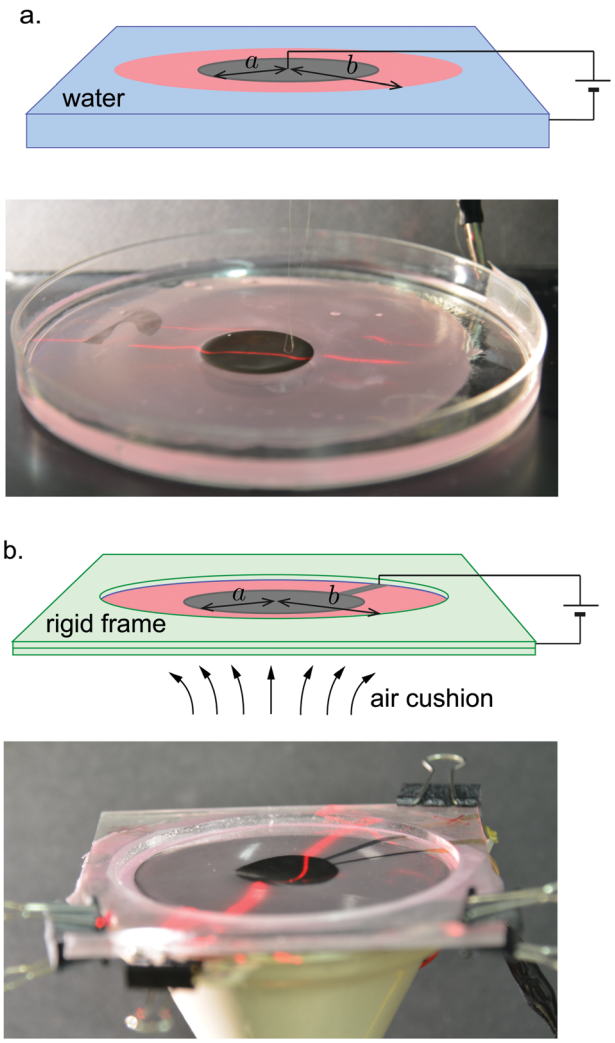

Fig. 2 Experimental configurations explored in this study. In both situations, the deflection of the membrane is monitored through the deviation of a laser sheet in oblique incidence. The black disk of radius *a* corresponds to the conductive part at the center of the pink membrane of radius *b*. (a) Disk floating on water. A single patch is coated on the upper side of the membrane and is connected to the generator. Water plays the role of the counter electrode and is connected to the ground. Surfactant molecules are added to the water to impose a fixed surface tension (of 30 mN m^{-1}) and increase the electric conductivity of the solution. (b) Disk clamped on a circular rigid frame. Conductive domains are symmetrically coated on both sides of the membrane. Air is gently blown from underneath to compensate for the weight of the membrane.

Nevertheless out-of-plane displacements of the membrane are limited by hydrostatic pressure. Using the analytical and numerical tools developed for this configuration, we investigate a second system where the membrane is clamped in a circular horizontal frame, the sagging effect of gravity being suppressed by applying a pressure Δp below the membrane (Fig. 2b). In contrast with most previous studies performed on thin pre-stretched DEAs that rely on nonlinear elasticity, we will use the weakly non-linear equations of thin elastic plates to investigate the buckled morphologies obtained with these configurations.

2 Spontaneous buckling of free floating plates

2.1 Dielectric membranes

The dielectric membranes used in the experiments are made of polyvinyl siloxane elastomers (Elite Double 8 from Zhermack). They are obtained by spin-coating a 4 ml mix of equal quantities of the ''catalyst'' and ''base'' liquids on a flat wafer of radius $b = 5$ cm. Using a spinning rate of 300 to 600 rpm for 15 s provides membranes of thickness h ranging from 100 to 300 μm. The Young's modulus of the polymer, $E = 250 \pm 15$ kPa, is estimated with a standard tensile test on a strip. Carbon black powder is manually deposited on the surface of the cured polymer with a brush through a circular stencil of radius a. The part covered with carbon black is referred to as the active part, whereas the remaining uncovered part of the membrane is designated as the passive part. The powder is applied until the black colour of the patch saturates. This coating is electrically conductive and its surface resistivity of a few hundred kΩ does not increase significantly upon additional applications of powder. Carbon black particles strongly adhere to the polymer so that the electrode preserves sufficient conductivity when stretched although we observe an increase of the resistivity of 500% for a typical strain of 40%. Nevertheless the resistivity recovers its initial value when the strain is released. The relative dielectric permittivity ε_r of PVS is accessed through a classical electrical measurement of the capacitance of a membrane coated with carbon black on both sides, leading to $\varepsilon_r = 2.5 \pm 0.6$.

2.2 Experimental setup

Once carbon black powder has been applied on the upper face, the membrane is gently deposited at the surface of a bath of soapy water where it floats freely. The surface tension of pure water is 72 mN m^{-1} but easily drops as low as 50 mN m^{-1} due to various pollutants. We deliberately add surfactants to impose a low but controlled surface tension $\gamma \simeq 30$ mN m^{-1} and enhance the electric conductivity of water. The voltage is imposed through a thin metallic wire (of radius of 10 μm) contacting lightly the circular electrode. The wire is connected to a high voltage amplifier (Trek model 609 – E) driven by a signal generator, while water is connected to the electrical ground and thus plays the role of a second compliant electrode. Indeed the charged carbon black electrode attracts opposite charges until the elastomer–water interface is equivalently charged. Voltages applied to the system typically range from 200 V to 5 kV. To measure out-of-plane deformations of the membrane, we use a laser sheet directed on the active part of the membrane with an oblique incidence. The deflections of the laser line are recorded using a camera placed above the setup and are directly proportional to the local vertical displacements of the membrane (Fig. 4). Note that all experiments (including the one of Section 4) are quasistatic. The applied voltage is increased with steps of 100 V for every 30 s, approximately. On these time scales, the response of PVS is purely elastic. Therefore we do not expect time to play any role in our experiments.

2.3 Electro-mechanical coupling

Applying an electric voltage V across the membrane results into two complementary effects: charges of the same sign exert an in-plane repulsion, whereas opposite charges attract each other through the thickness of the layer. Both contributions can be derived from energy considerations. The electrostatic energy of a capacitor is $\frac{1}{2}CV^2$, where C is the capacity. When the voltage V is fixed, an external generator provides an electrical work QV, where $Q = CV$ is the charge. The total electric energy under fixed voltage therefore reads for a planar capacitor:

$$\mathscr{W}_{\text{elec}} = \frac{1}{2}CV^2 - QV = -\frac{1}{2}\varepsilon_0\varepsilon_r V^2\frac{S}{h}$$

where $\varepsilon_0 = 8.85 \times 10^{-12}$ F m^{-1} is the vacuum permittivity and S the area of the electrode. Differentiating $\mathscr{W}_{\text{elec}}$ with respect to h (keeping S and V constant) shows that the charged electrodes apply a compressive pressure:

$$p_{\text{elec}} = \frac{1}{S}\frac{\partial U_{\text{elec}}}{\partial h} = \frac{1}{2}\varepsilon_0\varepsilon_r\left(\frac{V}{h}\right)^2$$

Similarly, differentiating $\mathscr{W}_{\text{elec}}$ with respect to S (keeping h and V constant) results in a term equivalent to a negative surface tension:

$$2\gamma_{\text{elec}} = \frac{\partial U_{\text{elec}}}{\partial S} = -\frac{1}{2}\varepsilon_0\varepsilon_r\frac{V^2}{h}$$

where the factor 2 accounts for the two coated interfaces when we extend the analogy with the tension in a soap film. Although the effect of surface tension is generally neglected in solid mechanics, capillarity may deform very soft objects as demonstrated in flourishing recent studies.[26,27]

What are the consequences of p_{elec} and γ_{elec} on a free membrane completely covered by an electrode (such as in Fig. 1)? Far from the edge, the effective negative surface tension results in a positive equibiaxial planar stress $\sigma_r = \sigma_\theta = -2\gamma_{\text{elec}}/h$. Besides, the electrical pressure leads to a compressive stress through the thickness, hence $\sigma_z = -p_{\text{elec}}$. The stresses in the membrane are therefore given by:

$$\sigma_r = \sigma_\theta = -\sigma_z = \frac{1}{2}\varepsilon_0\varepsilon_r\left(\frac{V}{h}\right)^2$$

For low enough deformations (in our experiment they are always less than 20%), linear Hooke's law applies and leads to the strain distribution:

$$e_r = e_\theta = \frac{-e_z}{1+2\nu} = \frac{1}{2E}\varepsilon_0\varepsilon_r\left(\frac{V}{h}\right)^2$$

where ν is the Poisson ratio of the material that constitutes the membrane.

The relevant terms of the strain tensor in setting the mechanics of a thin plate are limited to in-plane components $(e_r, e_\theta, e_{r\theta})$. The same in-plane strains are obtained when the plate is squeezed by a pressure $-\sigma_0$ and no surface tension, with

$$-\sigma_0 = \frac{1}{\nu}\frac{\varepsilon_0\varepsilon_r}{2}\left(\frac{V}{h}\right)^2 \quad (1)$$

This equivalent pressure $-\sigma_0 = p_{\text{elec}}/\nu$ is larger than the actual electrostatic pressure. In the particular case of elastomers, the value of ν is close to 1/2, and the whole strain distribution (including in this particular case the thickness strain e_z) is then correctly reproduced by assuming that the electrostatic pressure is doubled and that there is no effect of surface tension. This simplifying picture is used in most studies of dielectric actuation.[2,11,28] In this article, we study the case presented in Fig. 2a, where the electrodes (disk with radius a) do not cover entirely the elastic membrane (disk with radius $b \geq a$), and we show how this configuration can lead to buckling even if the boundaries of the membrane are free. In this more general problem, electrostatic forces can still be replaced by an equivalent pressure on the covering electrodes, even in non-planar solutions, as we demonstrate in another article[29] using variational methods.

In the following,

$$e_0 = -\frac{\nu}{E}\sigma_0 = \frac{1}{2E}\varepsilon_0\varepsilon_r\left(\frac{V}{h}\right)^2 \quad (2)$$

will be called the "actuation strain" which is the strain that an unconstrained piece of active membrane would achieve in the absence of external mechanical loading. Note finally that e_0 can be generalized to other types of deformations such as thermal expansion, swelling or even biological growth.

2.4 Membrane stresses in the flat configuration: below the buckling threshold

Using the equivalent pressure derived above, we now estimate the strain distribution in the freely floating membrane illustrated in Fig. 2a. As the membrane is deposited at the surface of water, surface tension forces tend to stretch it. The corresponding induced strain is γ/Eh, where γ is the surface tension of water ($\gamma \simeq 30$ mN m^{-1}, due to the presence of a surfactant in water), and is on the order of 10^{-3}. For a 200 μm thick membrane with free edges, an equivalent strain would be obtained when applying a voltage $(2\gamma h/\varepsilon_0\varepsilon_r)^{1/2} \sim 700$ V. The actual impact of surface tension is therefore significant. However, the mechanics of the membrane remain linear before buckling. If we consider this slightly prestretched state as a reference for the membrane, we should discard the effect of surface tension when we derive the stresses and strains induced by the electric field. In this linear regime, both effects are simply additive. Additivity nevertheless fails as the membrane buckles. In Section 3 the reference state is the unstrained membrane, and the effect of surface tension is taken into account. We assume that the problem remains axisymmetric and that the membrane only undergoes in-plane deformations. Mechanical equilibrium reads:

$$\frac{\partial r\sigma_r}{\partial r} - \sigma_\theta = 0 \quad (3)$$

We note $u(r)$ the radial displacement. We impose the effective pressure $-\sigma_0$ according to eqn (1) in the active domain. Using

$E^* = E/(1-\nu^2)$, Hooke's relation can be expressed as:

$$\sigma_r = E^*(e_r + \nu e_\theta) + \frac{\nu}{1-\nu}\sigma_z \quad (4)$$

$$\sigma_\theta = E^*(\nu e_r + e_\theta) + \frac{\nu}{1-\nu}\sigma_z, \quad (5)$$

and includes $\sigma_z = \sigma_0$ in the active domain, and $\sigma_z = 0$ in the passive zone. In the case of radial in-plane displacements, the radial and orthoradial strains are related to the radial displacement $u(r)$: $e_r = du/dr$ and $e_\theta = u/r$, respectively. Inserting these strains into eqn (3) leads to the differential equation, valid separately in both active and passive regions:

$$r^2u'' + ru' - u = 0. \quad (6)$$

where the symbol .′ stands for the derivative with respect to r. Solutions of Lamé's equations[30,31] are of the form $u(r) = \alpha r + \beta/r$, where the coefficients can be different in the active "A" ($r < a$) and passive "P" ($a < r < b$) zones and should be determined by matching the different boundary conditions.

We enforce the continuity of $u(r)$ and of $\sigma_r(r)$ (equilibrium condition) at the boundary $r = a$. The $1/r$ term should not be present in the active zone because of its divergence for $r = 0$. As a result, stresses and strains are equibiaxial in this region ($e_r = e_\theta = \alpha$ when $u = \alpha r$). Finally, this stress induced by activation vanishes at $r = b$ in the case of a freely floating membrane. Using these four conditions, we determine the corresponding constants α, β in both regions. We obtain in the active region the following displacement, strains and stresses:

$$u^A(r) = \frac{e_0}{2}(1-\nu)\left(\frac{a^2}{b^2} + \frac{1+\nu}{1-\nu}\right)r$$

leading to

$$e_r^A = e_\theta^A = \frac{e_0}{2}(1-\nu)\left(\frac{a^2}{b^2} + \frac{1+\nu}{1-\nu}\right) > 0$$

and

$$\sigma_r^A = \sigma_\theta^A = \nu\frac{\sigma_0}{2}\left(1 - \frac{a^2}{b^2}\right) < 0$$

In this area, strains are extensional, but lower than e_0, and stresses are compressive. Indeed, constraining the deformation of the active zone by a passive one logically results into compressive stresses. Similarly, the state of the passive zone is given by:

$$u^P(r) = e_0\frac{a^2}{2}\left((1-\nu)\frac{r}{b^2} + \frac{(1+\nu)}{r}\right)$$

so that:

$$\sigma_r^P = \nu\frac{\sigma_0}{2}\frac{a^2}{b^2}\left(\frac{b^2}{r^2} - 1\right) < 0$$

$$\sigma_\theta^P = -\nu\frac{\sigma_0}{2}\frac{a^2}{b^2}\left(1 + \frac{b^2}{r^2}\right) > 0$$

In this passive region, the radial stress is compressive, whereas the orthoradial stress is tensile, both stresses decaying away from the active patch (note the strong discontinuity in orthoradial stress and in radial strain at the boundary $r = a$).

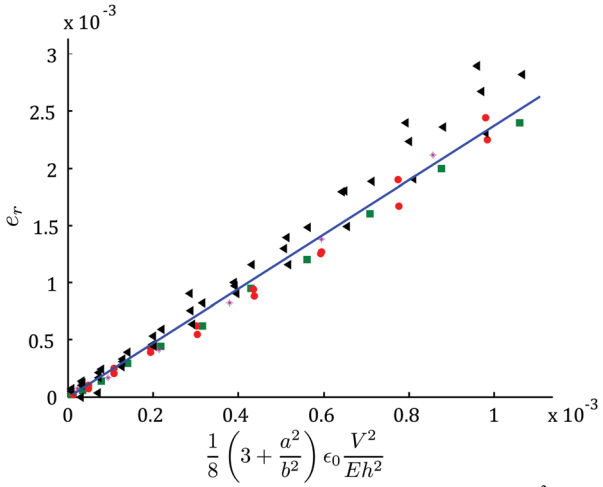

Fig. 3 Radial strain in the active zone as a function of $\frac{1}{8}\left(3+\frac{a^2}{b^2}\right)\left(\frac{\varepsilon_0 V^2}{E h^2}\right)$ for different thicknesses: (✳) h = 150 μm, (●) h = 210 μm, (■) h = 250 μm, (◀) h = 260 μm. The slope corresponds to the relative dielectric constant of the polymer (ε_r = 2.4).

A calibration of the electromechanical response of the membranes requires a precise estimation of the strain field, which is carried out through Digital Image Correlation (DIC). Talc powder is lightly sputtered on the surface of the membrane in order to obtain random spots of typical size 50 μm. Pictures of the membrane are taken using a digital camera with a resolution of 20 μm per pixel. We use Correli DIC software[32] to obtain the deformations $e_r = e_\theta$ of the membrane in the active zone ($r/a < 1$). In order to validate the theoretical description, we finally plot e_r as a function of the theoretical strain divided by ε_r: $e_r^{theo}/\varepsilon_r = \frac{1}{8}\left(3+\frac{a^2}{b^2}\right)\left(\frac{\varepsilon_0 V^2}{E h^2}\right)$, for $\nu = 1/2$. Within low enough strains, the experimental strains obtained for several values of a and h collapse on a straight line of slope $\varepsilon_r = 2.4 \pm 0.1$, which confirms our electrical measurements (see Fig. 3). However, it is visible that collapse starts to deteriorate for higher strains. This scatter might be due to some non-linear effect (including the buckling of the membrane), or to a systematic error on the measurement. In the following section, we describe the buckling threshold and the deflection of the membrane.

3 Out of plane buckling

3.1 Experimental observations

As the applied voltage is increased, the active part tends to expand, in conflict with the external passive zone so that radial compressive stresses build up along the whole membrane. As a consequence, the membrane undergoes an axisymmetric buckling instability above a critical applied voltage. In contrast with classical Euler buckling where a compressed beam is bent along its whole length, we observe that buckling is localized inside the active zone in the vicinity of its boundary (Fig. 4a). We also observe that the global mode of the instability depends on the size of the active zone.

Rising the voltage beyond the buckling threshold induces an increase of the amplitude but does not modify this mode (Fig. 4b).

The deflection of the membrane is limited by its bending rigidity and also by the hydrostatic pressure of the underneath water. As in other systems involving compressed floating sheets, we expect buckling modes to be dictated by a competition between bending stiffness and gravity.[33,34] Balancing both effects leads to an elastogravity length scale, $\ell_{eg} = 2\pi\left(\frac{Eh^3}{12(1-\nu^2)\rho g}\right)^{1/4}$, which sets the wavelength of the incipient buckling mode of a long 1D strip floating on water. For a typical membrane of thickness h = 200 μm, we obtain $\ell_{eg} \approx$ 1.4 cm. In Fig. 4a, we use ℓ_{eg} as a scale bar. We observe that the buckling pattern is localized and the width of the corresponding annulus is comparable with this length scale for $a \gg \ell_{eg}$. Conversely, the deformation involves the whole diameter of the active zone for lower values of a. To assess the onset of the buckling threshold and its evolution, we monitor the profile as a function of the applied voltage (Fig. 4b). We characterize this actuation by the actuation strain e_0 (see eqn (2)) that we compare with the critical compressive strain leading to the buckling of a long 1D strip lying on water, $e_{1D} = \left(\frac{\rho g h(1-\nu^2)}{3E}\right)^{1/2} = \frac{2\pi^2}{3}\left(\frac{h}{\ell_{eg}}\right)^2$. Results are displayed as dots in Fig. 5. The evolution of the amplitude is not as sharp as in the case of a classical pitchfork transition that we would expect for the buckling of the membrane. We interpret this smoother transition as a consequence of imperfections, due for instance to a slight deformation of the membrane caused by its contact with the wire and to the possible migration of charges outside the active region. A critical applied voltage (*i.e.* a critical actuation strain in the graph) for the buckling threshold can nevertheless be estimated. In the following section we develop the non-linear equations describing this electro-activated buckling.

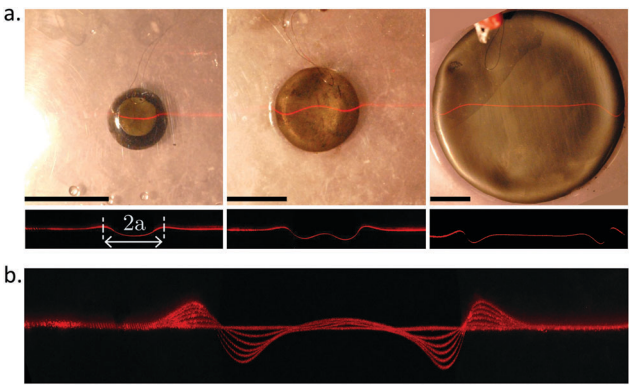

Fig. 4 (a) Different buckling profiles at V = 5 kV and h = 210 μm, for different radii of the active zone (from left to right: a = 0.5 cm, a = 1 cm, a = 3 cm). The upper row is a picture of the membrane taken from above, while the lower one highlights the profile of the membrane. Scale bar: elastogravity length scale $\ell_{eg} = 2\pi\left(\frac{Eh^3}{12(1-\nu^2)\rho g}\right)^{1/4} \approx 1.4$ cm. (b) Superposition of laser profiles obtained for increasing applied voltage (from 0 kV to 5 kV, h = 210 μm, a = 1.5 cm). While the amplitude of the instability increases progressively, the global buckling mode remains the same.

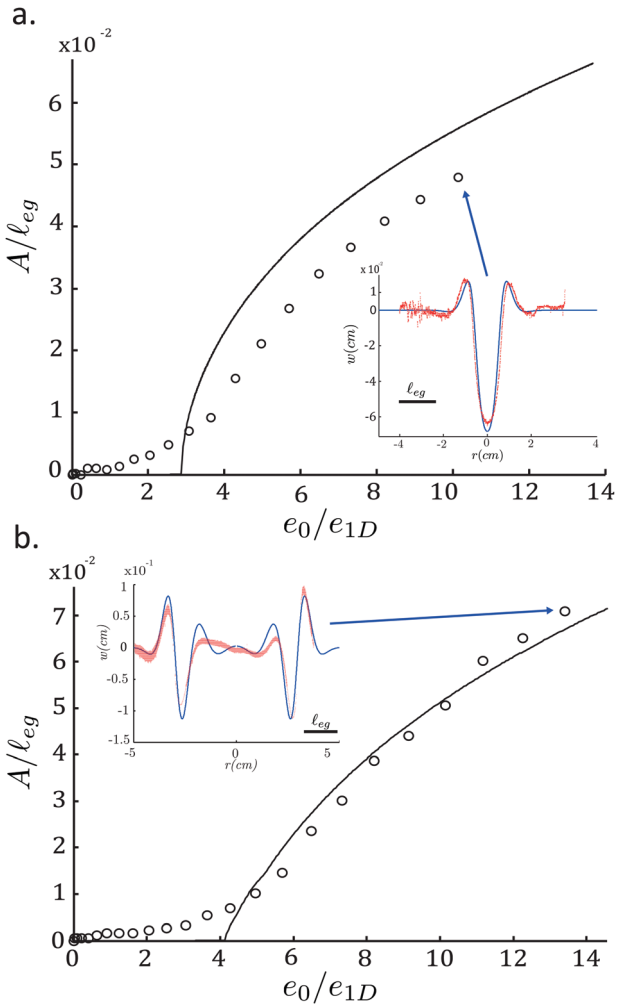

Fig. 5 Maximal amplitude A of the deflection normalized by ℓ_{eg} as a function of the applied voltage characterised by e_0/e_{1D}. Experimental data (circles) are compared to numerical integration of eqn (7) and (8) (continuous line) for a membrane of thickness 200 μm. We did not use any fitting parameter. Inset: Superposition of numerical (blue) and experimental (red) profiles at the point indicated by the arrow. (a) a = 6 mm, (b) a = 30 mm.

3.2 Non-linear equations for the buckled state

We now describe the buckling and post-buckling evolution of the system, using axisymmetric weakly non-linear plate equations. Because strains remain low in our experiments, we will consider the whole system as a plate with a uniform thickness. We also follow the assumption of Föppl–Von Kármán plate equations which considers that out-of-plane displacement $w(r)$ is coupled to in-plane strains.[30] We first write the equilibrium of membrane stresses in the frame of reference of the plate, assuming that the slope is small ($w' \ll 1$). The radial strain now reads $e_r = u' + w'^2/2$, while $e_\theta = u/r$ remains unchanged. Using Hooke's relations (eqn (4) and (5)), in-plane equilibrium in eqn (3) now leads to:

$$r^2u'' + ru' - u + \frac{1-\nu}{2}rw'^2 + r^2w'w'' = 0. \qquad (7)$$

which is valid separately in the active and in the passive zone. The second equation accounts for the torque balance of the plate, which in this axisymmetric case reads:[35]

$$D\Delta^2 w = N_r w'' + N_\theta \frac{w'}{r} + q \qquad (8)$$

where $D = \frac{Eh^3}{12(1-\nu^2)}$ is the flexural rigidity, and $N_r = h\sigma_r$ and $N_\theta = h\sigma_\theta$ are the in-plane forces per unit length, which contain the electrical actuation, since they derive from eqn (4) and (5). The last term $q = -\rho g w$ corresponds to the hydrostatic pressure of the lifted water. In addition to the boundary conditions mentioned in the previous section, 4 other conditions have to be implemented to solve the non-linear coupled differential eqn (7) and (8).[34] Symmetry imposes $w'(0) = w'''(0) = 0$. The effect of surface tension is taken into account through in-plane stresses applied as boundary conditions. At the edge of the membrane, the radial tension balances the surface tension of water $N_r(b) = \gamma$ and in the absence of momentum the curvature along the radial direction vanishes, $w''(0) = 0$. We solve these coupled system equations using the bvp4c routine from Matlab.

3.3 Numerical results *versus* experiments

For high enough loads, out-of-plane equilibrium profiles of the membrane are obtained. We represent in the inset of Fig. 5 the profiles calculated (without any adjustable parameter) for the highest values of e_0 achieved experimentally: $V = 4000$ V, *i.e.* $e_0 = 1.7 \times 10^{-2}$ for $a = 6$ mm and $V = 5000$ V, *i.e.* $e_0 = 2.7 \times 10^{-2}$ for $a = 30$ mm. Both profiles are non-dimensionalized by ℓ_{eg} and compared with the corresponding experimental profiles (in red). The agreement between experiments and numerical calculations is fairly good although the small oscillations predicted for the wider active zone are not perfectly observed in the experiment. We interpret this minor discrepancy as a consequence of slight inhomogeneities of the membrane. We determine the maximum amplitude of the calculated profile for decreasing loads and compare it to the experimental data (Fig. 5). Although the numerical estimation reasonably matches the experimental data, the predicted transition to the out-of-plane state is sharper than the experimental one as we would expect for a perfect bifurcation instability.

Since our model captures correctly the physics of the problem, we now use it to determine how the buckling threshold depends on the size of the active region. Dimensional analysis of eqn (4)–(8) shows that the normalized critical actuation strain e_{0c}/e_{1D} should be a function of Poisson's ratio ν and the two non-dimensional parameters $(a/b, \ell_{eg}/b)$ if the surface tension of water is neglected. The additional traction induced to the membrane by capillarity tends to increase the threshold and involves an extra non-dimensional parameter $\gamma b^2/\rho g \ell_{eg}^4$. We represent in Fig. 6 the prediction of the threshold e_{0c}/e_{1D} as a function of the aspect ratio a/b for a particular case relevant for our experiments corresponding to $h = 210$ μm and $b = 5$ cm, *i.e.* ($\ell_{eg}/2b = 0.14$ and $\gamma b^2/\rho \ell_{eg}^4 = 7.8$). Note that this plot is not universal and is shifted for different values of the two non-dimensional parameters.

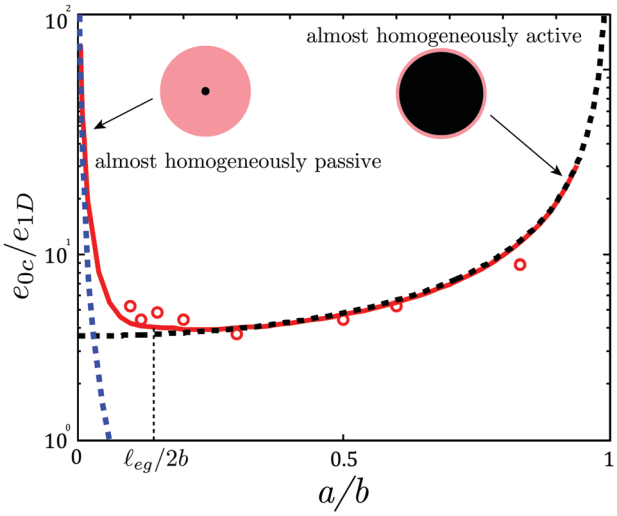

Fig. 6 Normalized critical buckling (actuation strain as a function of the aspect ratio for the particular case $h = 210$ μm and $b = 5$ cm (*i.e.* $\ell_{eg}/2b = 0.14$ and $\gamma b^2/\rho \ell_{eg}^4 = 7.8$). Red line: numerical resolution of eqn (4)–(8). Circles: experimental data. Blue dotted line: fit with the simplified form (eqn (9)) $f(x) = -\frac{3.3 \times 10^{-3}}{x^2(x^2-1)}$ corresponding to the limit $2a \ll \ell_{eg}$ (*i.e.* $a/b \ll 0.07$ for our system). Black dotted line: fit with the simplified form (eqn (10)) $g(x) = \frac{3.62}{1-x^2}$ corresponding to the opposite limit $2a \gg \ell_{eg}$.

Two regimes may be identified as the diameter of the active zone is compared with ℓ_{eg}.

(i) In the case $2a \ll \ell_{eg}$, the membrane buckles along a length scale a. In terms of orders of magnitude, the critical stress is expected to scale as $\sigma_c \sim -E\frac{h^2}{a^2}$ as in classical Euler buckling.[36] If we use the stress computed for the active region before buckling, $\sigma_r = \frac{1}{2}Ee_0\left(\frac{a^2}{b^2} - 1\right)$, we deduce:

$$e_{0c} \sim \frac{h^2}{a^2}\frac{1}{1-\frac{a^2}{b^2}} \quad i.e. \quad \frac{e_{0c}}{e_{1D}} \sim \left(\frac{\ell_{eg}}{b}\right)^2 \frac{1}{\frac{a^2}{b^2}\left(1-\frac{a^2}{b^2}\right)} \qquad (9)$$

This expression is represented by the blue dashed line in Fig. 6 with a fitting prefactor to match the numerical results. This simplified scaling law thus correctly captures the divergence of critical active strain for buckling as the size of the active zone vanishes.

(ii) In the opposite case $2a \gg \ell_{eg}$, buckling occurs on a typical size ℓ_{eg}. The critical stress is now expected to scale as $\sigma_c \sim -E\frac{h^2}{l_{eg}^2}$, which leads for the critical actuation strain:

$$\frac{e_{0c}}{e_{1D}} \sim \frac{1}{1-\frac{a^2}{b^2}} \qquad (10)$$

This relation is plotted as a black dashed line in Fig. 6 with a numerical prefactor fitted to the numerics. The matching with the numerically computed threshold is very good. As intuitively expected, the critical actuation strain diverges in both limits

$a \to 0$ and $a \to b$, where the system is almost homogeneous. In the first limit, stronger stresses are required as smaller buckling lengths are considered. Conversely, buckling tends to be suppressed as the constraining role of the passive zone gets relatively weaker. We note finally that the buckling threshold is nearly constant in the range $\ell_{eg}/2 < a < 0.7b$, $e_c \simeq 0.5e_{1D}$. In this limit, the compressive stresses due to activation are indeed on the order of $\sigma_r \sim Ee_0$ (independently of a/b), and have to match the critical buckling stress $\sigma_c \sim Ee_{1D}$. Our experimental data lie mostly in this regime (circles in Fig. 6). They are in fair agreement with these predictions without any adjustable parameter.

4 Buckling of clamped plates

The previous floating free configuration is interesting as a model case since the different physical ingredients leading to the buckling instability can be precisely quantified. However, most practical applications involve a membrane held on a frame. In this section, we study the buckling of a clamped membrane, subjected to a non homogeneous voltage distribution. In contrast with many studies from the literature conducted with highly prestretched membranes,[2,37] we tried to limit prestress as much as possible. We will nevertheless evaluate how slight residual stresses may modify significantly the mechanical behaviour of the membrane.

4.1 Experimental set-up and preliminary observations

The membranes are prepared following the same procedure as in the previous configuration. Opposite conductive patches of radius a are now coated on each side of the membrane. In order to limit possible strains due to the manipulation of the membrane during the framing step, we lay an annulus cut in thick paper on the spin-coated layer before curing. The liquid polymer penetrates the paper, which enhances the adhesion of the cured membrane on the flexible paper frame. The reinforced membrane can then be peeled and manipulated without inducing additional strain. The polymeric sheet is finally clamped in a rigid acrylic frame with a circular opening of radius $b = 5$ cm and held horizontally. The membrane would tend to sag over its own weight leading to an induced strain on the order of $(\rho_p gR/E)^{2/3} \sim 2.5 \times 10^{-2}$, where ρ_p is the density of the polymer. This strain is large compared with the typical buckling strain, as we will see. Therefore, in order to compensate for this additional tension, we gently blow air from underneath. The pressure of this air cushion is tuned until the profile of the membrane monitored with the laser sheet appears uniformly flat (Fig. 2b). First experimental observations show that buckling occurs beyond a critical voltage that decreases as wider active domains are considered. We also observe that the buckled profiles obtained with this configuration take the axisymmetric shape of a dome localised in the active region. In the following section we compare the observed profiles with the theoretical framework adapted from the previous free floating configuration.

4.2 Theoretical buckling in the clamped membranes

The equations dictating the shape of the membrane are the same as in the previous configuration. In the absence of hydrostatic pressure, the q term in eqn (8) now vanishes. Clamping the membrane in a frame also modifies the boundary conditions: $u(r = b) = w(r = b) = w'(r = b) = 0$. Using these equations, we calculate the critical buckling actuation strain e_{0c} for values of a/b ranging from 0.01 to 1. This last case corresponds to the classical derivation from Timoshenko:[36] $e_{0c} \simeq \frac{14.7}{12(1-\nu^2)}\frac{h^2}{a^2} \simeq 0.82\frac{h^2}{a^2}$. We thus represent in Fig. 7 the value of e_{0c} normalized by $(h/a)^2$ as a function of a/b. The data from the numerics are well represented by an empirical relation:

$$e_{0c} = \frac{h^2}{a^2}\left(0.27 + 0.56\frac{a}{b}\right) \quad (11)$$

Counter-intuitively, buckling is relatively easier for a small patch than for a wider one. Indeed, out of plane deformation is not strictly bound to the active zone and can also involve part of the passive one, leading to a lower buckling threshold.

The buckling actuation strain measured in our experiments is however 5 to 100 times higher than expected from these numerical calculations (Fig. 8). We interpret this significant shift as due to the prestrain induced during the curing stage.[38] We estimate this strain through DIC by comparing a membrane initially clamped to a paper frame and then released. We evidence a prestrain e_p on the order of 2×10^{-3}, which is large in comparison with typical values predicted for the buckling strain ($e_{0c} \sim 10^{-3}$). As a conclusion, although the paper frame limits additional non-uniform prestrains due to the manipulation of the membrane, a uniform prestrain is still present in the samples. In the following section, we therefore include an initial extensional prestrain e_p in the calculation to better capture the features experimentally observed.

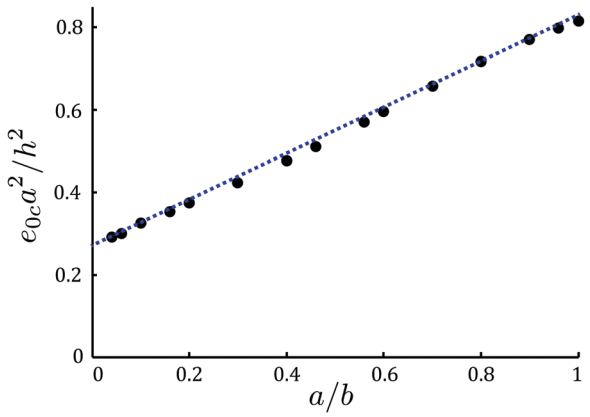

Fig. 7 Numerical prediction of the normalized critical buckling strain $e_{0c}a^2/h^2$ as a function of the aspect ratio a/b, for a clamped plate, in the absence of gravity or prestrain. The data are well fitted by a linear regression: $e_{0c} = \frac{h^2}{a^2}\left(0.27 + 0.56\frac{a}{b}\right)$. For $a = b$, we recover Timoshenko's classical result $e_{0c} \sim 0.83\frac{h^2}{a^2}$ for the buckling of a clamped disk.

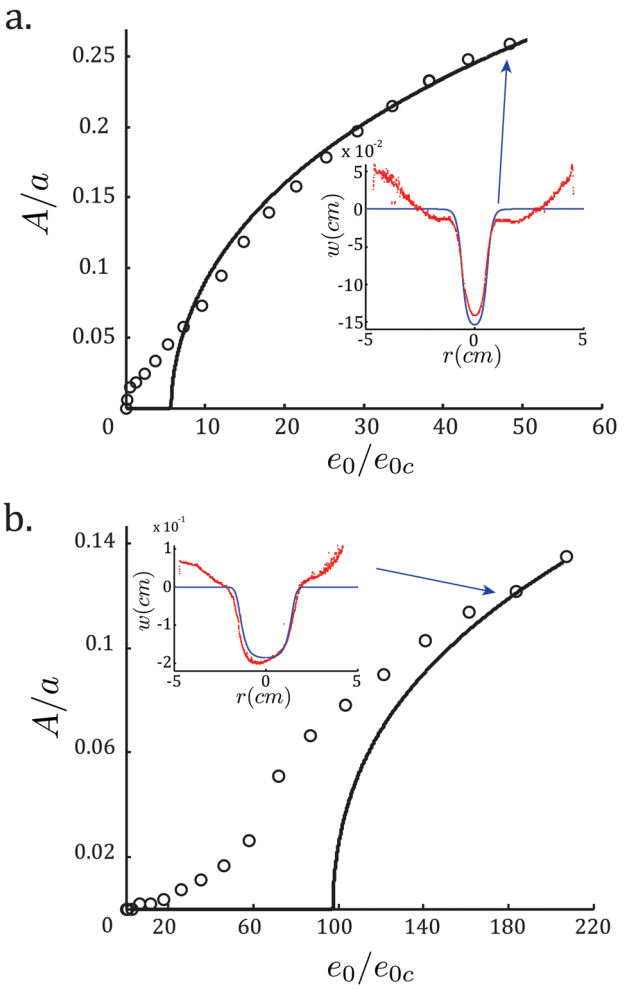

Fig. 8 Circles: normalized amplitude of the deflection A/a as a function of the applied strain normalized by the value predicted by eqn (11) e_0/e_{0c}. Continuous line: numerical resolution (eqn (7)–(8)). Inset: Superposition of numerical (blue line) and experimental profiles (red dots) for the point indicated by the arrow. (a) h = 150 μm, a = 6 mm, e_p = 0.0007, e_c = 2.11 × 10^{-4} (inset V = 3600 V, *i.e.* e_0 = 0.03). (b) h = 150 μm, a = 15 mm, e_p = 0.004, e_c = 4.38 × 10^{-4} (inset V = 3400 V, *i.e.* e_0 = 0.027).

4.3 Comparison of the amplitude and the mode shape

As in the previous floating configuration, the profiles of the membranes are deduced from the deflection of the laser line (insets in Fig. 8). Membranes are mainly deformed in the active region, although residual sagging is also present in the passive part. We also plot the normalized amplitude of the deflection A/a as a function of the applied strain normalized by the predicted value corresponding to eqn (11) (without any prestrain). The bifurcation is quite imperfect and extrapolated thresholds are 5 to 100 times larger than expected. In order to provide a better comparison between the numerical resolution of eqn (7) and (8) and the experimental data, we added a uniform prestrain e_p, which results in a boundary condition $N_r(r=b)=\frac{Eh}{1-\nu}e_p$. For each sample e_p is tuned to obtain a good match between the calculated and observed profiles.

The fitting prestrain values range from 7 × 10^{-4} to 4 × 10^{-3}, which is in agreement with the values obtained through DIC.

The comparison between experiments and numerical calculations shows us the important impact of prestrain on the buckling behaviour of the membrane that we study in more detail in the following section.

4.4 Buckling in a prestretched membrane

In the absence of prestrain, the radial stress in the active region is given, before buckling, by the integration of eqn (3)–(6) (in-plane deformation): $\sigma_r=\frac{E}{1-\nu}\left[-e_0\left(\frac{1+\nu}{2}\left(\frac{a^2}{b^2}-1\right)+1\right)\right]$. Adding a prestrain e_p shifts the stress by the quantity $\sigma_r^p=\frac{E}{1-\nu}e_p$. We plot in Fig. 9 the critical actuation strain e_{0c} as a function of $(h/a)^2$ for different values of the prestrain and a fixed aspect ratio a/b = 0.1. Without prestrain e_{0c} varies linearly with $(h/a)^2$ for a fixed value of a/b as commented in Fig. 7. One obvious consequence of the prestrain is to shift the critical load to higher values as expected from the shift in stresses. For a better comparison, we define an effective strain $e = e_0 - \eta e_p$, with $\eta=\left(\frac{1+\nu}{2}\left(\frac{a^2}{b^2}-1\right)+1\right)^{-1}\simeq 3.9$, which accounts for the prestrain. Hence, when $e > 0$ the voltage induced strain is

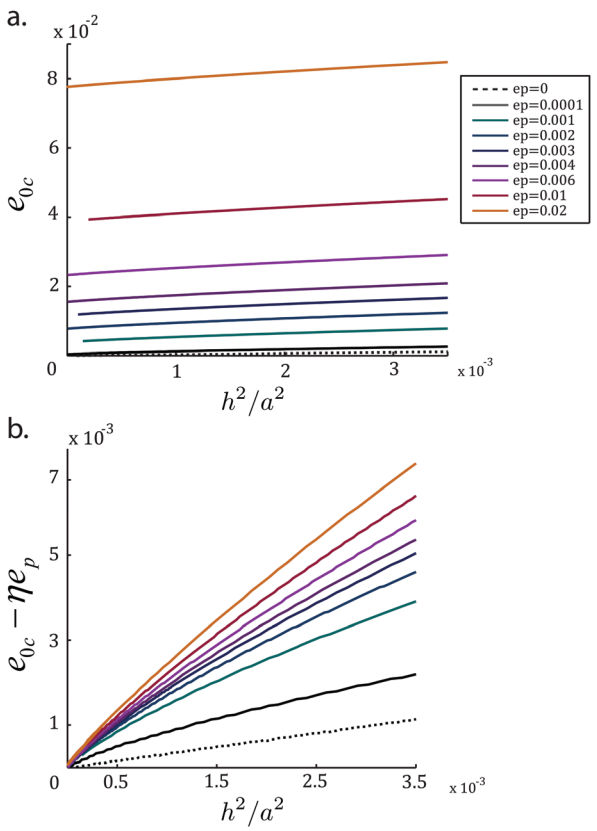

Fig. 9 Numerical study of the effect of the prestrain on the buckling threshold. (a) Buckling threshold e_{0c} as a function of $(h/a)^2$ for different values of the prestrain. The aspect ratio a/b is arbitrary set to 0.1 for all cases. (b) Evolution of the effective strain $e_c - \eta e_p$ as a function of $(h/a)^2$ for various values of the prestrain. For e_p = 0 (dashed line) e_c varies linearly with $(h/a)^2$. However this proportionality is lost when $e_p > 0$.

compressive enough to compensate for the initial prestrain. The plots of effective strain at buckling as a function of h^2/a^2 do not collapse on a same master curve and the linear dependence with $(h/a)^2$ is lost. The effect of prestrain is therefore not simply additive. Indeed, the stresses induced by the electrostatic loading are not equi-biaxial in the passive part of the membrane, and therefore do not simply compensate the prestress. This effect is modest in the present case, however practical applications can involve highly prestretched membranes to avoid pull-in instabilities. Although exploring the non-linear elastic domain is beyond the scope of the current work, we highlighted the fact that the consequences of prestrain in activated membranes are non-trivial.

4.5 Secondary buckling bifurcation

So far, our experiments were restricted to the limit of small slopes $w' \ll 1$, *i.e.* to moderate applied loads. Although non-linear buckling instabilities were observed, axisymmetry was maintained in the observed patterns. An interesting secondary instability is however observed in the last case of membranes held on a rigid frame. Beyond a second critical voltage, azimuthal wrinkles appear at the border of the active zone (Fig. 10). Within the range of our experimental parameters (V is limited to 5 kV), these wrinkles are only observed for sufficiently large active patches (typically $a > 1.5$ cm for $h = 150$ μm). Provided that the prestrain in the membrane is sufficiently homogeneous (and low), their wavelength is well-defined and does not evolve significantly with the applied voltage. We did not observe the secondary instability with the membrane floating on water, presumably because we were not able to reach higher voltages with our setup. The observed pattern is very reminiscent of the wrinkles observed when inflating a mylar balloon[39] or at the edges of a very thin sheet deposited at the curved surface of a droplet of water.[40] Similar wrinkles have been reported in dielectric polymers as the load is released after a very high deformation.[14] Such wrinkles are the consequence of compressive orthoradial stresses. Numerical calculations of the azimuthal stress σ_θ indeed show the presence of high compressive stress at the edges of the active zone. Nevertheless the description of the buckling threshold and the value of the observed wavelength still remain open questions.

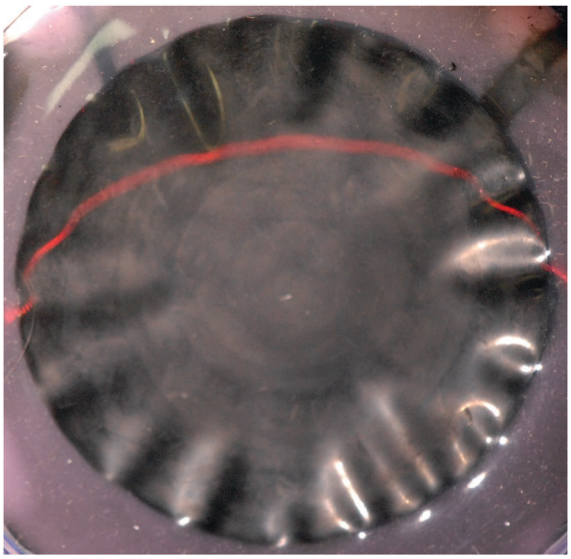

Fig. 10 Secondary instability leading to regular azimuthal wrinkles near the edges of the active region (a = 3 cm, h = 150 μm, V = 5 kV).

5 Concluding remarks

We have shown in this study how a non-uniform voltage distribution can trigger buckling instabilities in free floating, or clamped dielectric elastomeric sheets. In the first configuration, the interplay between hydrostatics and the bending stiffness of the membrane provides a length scale to the problem. If the diameter of the active zone is large in comparison with this elastogravity length, the buckling is localized in the vicinity of the border of the active zone. The typical width of the wrinkles is then set by the elastogravity length. In the opposite situation, a dimple is formed at the center of the buckled active zone. We find that the instability is favored (lower threshold) when actuation is truly heterogeneous: almost fully active or fully passive configuration is less prone to buckling (see Fig. 6).

In the second configuration the membrane is clamped in a frame. In the absence of gravity, the relevant length scale becomes the size of the system and more specifically, the diameter of the active zone. A first bifurcation then leads to the out-of-plane buckling of the active zone into an axisymmetric dome. For higher voltages, we observe a secondary instability: azimuthal wrinkles appear at the border of the active zone and grow as the voltage is further increased. In both configurations, buckling mechanics can be captured by solving the Föppl–Von Kármán equations in which the electrical effect is rendered through an "actuation" strain proportional to the square of the applied voltage. We validated this numerical approach with a fair comparison with our experimental results. Using this tool, we could study in detail the effect of a small prestrain in the buckling behaviour of the membranes. However, further work will probably be necessary to extend our study to the very large prestrain applied in many studies.

We believe that our results constitute a first step towards the use of dielectric elastomers as model systems to study mechanical instabilities triggered by non-uniform in-plane actuation. Applying a voltage modifies the metrics of the dielectric membrane in the same manner as thermal expansion, swelling or biological growth would. In terms of applications, such actuators could be used to obtain 3D shapes through electromechanical instabilities.

Acknowledgements

This work was partially funded by the Interuniversity Attraction Poles Programme (IAP 7/38 MicroMAST) initiated by the Belgian Science Policy Office and the French ANR SMArT.

We thank Bruno Sécordel for his initial experiments with dielectric membranes that lead to this study.

References

1 C. Keplinger, M. Kaltenbrunner, N. Arnold and S. Bauer, *Proc. Natl. Acad. Sci. U. S. A.*, 2010, **107**, 4505–4510.
2 R. Pelrine, R. Kornbluh, Q. Pei and J. Joseph, *Science*, 2000, **287**, 836–839.
3 J. Huang, T. Li, C. Chiang Foo, J. Zhu, D. R. Clarke and Z. Suo, *Appl. Phys. Lett.*, 2012, **100**, 041911.
4 F. Carpi and D. D. Rossi, *Bioinspiration Biomimetics*, 2007, **2**, S50–S63.
5 F. Carpi, G. Frediani, S. Turco and D. De Rossi, *Adv. Funct. Mater.*, 2011, **21**, 4152–4158.
6 O. A. Araromi, I. Gavrilovich, J. Shintake, S. Rosset, M. Richard, V. Gass and H. R. Shea, *ASME Transactions on Mechatronics*, 2015, **20**, 438–446.
7 J. Shintake, S. Rosset, B. Schubert, D. Floreano and H. Shea, *Adv. Mater.*, 2016, **28**, 231–238.
8 B. M. O'Brien, E. P. Calius, T. Inamura, S. Q. Xie and I. A. Anderson, *Appl. Phys. A: Mater. Sci. Process.*, 2010, **100**, 385–389.
9 C. Foo, S. J. A. Koh, C. Keplinger, R. Kaltseis, S. Bauer and Z. Suo, *J. Appl. Phys.*, 2012, **111**, 094107.
10 J. Huang, S. Shian, Z. Suo and D. R. Clarke, *Adv. Funct. Mater.*, 2013, **23**, 5056–5061.
11 Z. Suo, *Acta Mech. Solida Sin.*, 2010, **23**, 549–578.
12 J. Zhu, M. Kollosche, T. Lu, G. Kofod and Z. Suo, *Soft Matter*, 2012, **8**, 8840–8846.
13 C. Keplinger, T. Li, R. Baumgartner, Z. Suo and S. Bauer, *Soft Matter*, 2012, **8**, 285–288.
14 G. Mao, X. Huang, M. Diab, T. Li, S. Qu and W. Yang, *Soft Matter*, 2015, **11**, 6569–6575.
15 X. Liang and S. Cai, *J. Appl. Mech.*, 2015, **82**, 101002.
16 H. Zhao, J. Zhao, J.-W. Zha, Z.-F. Zhang, D.-R. Wang and Z.-M. Dang, *J. Adv. Phys.*, 2013, **2**, 13–19.
17 Q. Wang and X. Zhao, *Phys. Rev. E: Stat., Nonlinear, Soft Matter Phys.*, 2013, **88**, 042403.
18 X. Zhao and Q. Wang, *Appl. Phys. Rev.*, 2014, **1**, 021304.
19 B. Tavakol, M. Bozlar, C. Punckt, G. Froehlicher, H. A. Stone, I. A. Aksay and D. P. Holmes, *Soft Matter*, 2014, **10**, 4789–4794.
20 S.-i. Son, D. Pugal, T. Hwang, H. R. Choi, J. C. Koo, Y. Lee, K. Kim and J.-D. Nam, *Appl. Opt.*, 2012, **51**, 2987–2996.
21 P. Chakraborti, H. K. Toprakci, P. Yang, N. Di Spigna, P. Franzon and T. Ghosh, *Sens. Actuators, A*, 2012, **179**, 151–157.
22 S. Vishniakou, B. W. Lewis, X. Niu, A. Kargar, K. Sun, M. Kalajian, N. Park, M. Yang, Y. Jing, P. Brochu, Z. Sun, C. Li, T. Nguyen, Q. Pei and D. Wang, *Sci. Rep.*, 2013, **3**, 2521.
23 J. Dervaux and M. Ben Amar, *Phys. Rev. Lett.*, 2008, **101**, 068101.
24 Z. L. Wu, M. Moshe, J. Greener, H. Therien-Aubin, Z. Nie, E. Sharon and E. Kumacheva, *Nat. Commun.*, 2013, **4**, 1586.
25 J. Kim, J. A. Hanna, M. Byun, C. D. Santangelo and R. C. Hayward, *Science*, 2012, **335**, 1201–1205.
26 E. R. Jerison, Y. Xu, L. A. Wilen and E. R. Dufresne, *Phys. Rev. Lett.*, 2011, **106**, 186103.
27 S. Karpitschka, A. Pandey, L. A. Lubbers, J. H. Weijs, L. Botto, S. Das, B. Andreotti and J. H. Snoeijer, *Proc. Natl. Acad. Sci. U. S. A.*, 2016, **113**, 7403–7407.
28 P. Ronald, K. Roy and J. Jose, *Sens. Actuators, A*, 1998, **64**, 77–85.
29 H. Bense, B. Roman, J. Bico and B. Andreotti, in prep., 2017.
30 S. Timoshenko and S. Woinowsky-Krieger, *Theory of plates and shells*, McGraw-Hill, 2nd edn, 1959.
31 B. Audoly and Y. Pomeau, *Elasticity and Geometry: From hair curls to the non-linear response of shells*, OUP Oxford, 2010.
32 http://www.correli-stc.com/.
33 L. Pocivavsek, R. Dellsy, A. Kern, S. Johnson, B. Lin, K. Y. C. Lee and E. Cerda, *Science*, 2008, **320**, 912–916.
34 M. Piñeirua, N. Tanaka, B. Roman and J. Bico, *Soft Matter*, 2013, **9**, 10985–10992.
35 E. H. Mansfield, *The bending and stretching of plates*, Cambridge university press, 1989.
36 S. Timoshenko and J. Gere, *Theory of elastic stability*, Dover, 2nd edn, 1961.
37 S. Bauer, S. Bauer-Gogonea, I. Graz, M. Kaltenbrunner, C. Keplinger and R. Schwödiauer, *Adv. Mater.*, 2014, **26**, 149–162.
38 Y. Xia and G. M. Whitesides, *Annu. Rev. Mater. Sci.*, 1998, **28**, 550–575.
39 W. H. Paulsen, *The American Mathematical Monthly*, 1994, **101**, 953–958.
40 H. King, R. D. Schroll, B. Davidovitch and N. Menon, *Proc. Natl. Acad. Sci. U. S. A.*, 2012, **109**, 9716–9720.

